Polysulfide-mediated solvation shell reorganization for fast Li$^+$ transfer probed by *in-situ* sum frequency generation spectroscopy

Jian Wang [a,b,c,1,*], Haitao Liu [d,1], Jing Zhang [e], Qingbo Xiao [a], Chong Wang [f], Yongzheng Zhang [g], Meinan Liu [a], Qi Kang [h], Lujie Jia [a], Dong Wang [i], Qi Li [b,c], Wenhui Duan [f], Henry Adenusi [j,k,l], Stefano Passerini [b,c,m,**], Yuegang Zhang [f,**], Hongzhen Lin [a,*]

[a] *i-Lab & CAS Key Laboratory of Nanophotonic Materials and Devices, Suzhou Institute of Nano-Tech and Nano-bionics, Chinese Academy of Sciences, Suzhou 215123, China*
[b] *Helmholtz Institute Ulm (HIU), Ulm D89081, Germany*
[c] *Karlsruhe Institute of Technology (KIT), Karlsruhe D-76021, Germany*
[d] *Laboratory of Computational Physics, Institute of Applied Physics and Computational Mathematics, Beijing 100088, China*
[e] *School of Materials Science and Engineering, Xi'an University of Technology, Xi'an 710048, China*
[f] *Department of Physics, Tsinghua University, Beijing 100084, China*
[g] *State Key Laboratory of Chemical Engineering, East China University of Science and Technology, Shanghai 200237, China*
[h] *Department of Polymer Science and Engineering, Shanghai Jiao Tong University, Shanghai 200240, China*
[i] *Key Laboratory of Automobile Materials of MOE, School of Materials Science and Engineering, Jilin University, Changchun 130012, China*
[j] *Department of Science and Engineering of Matter, Environment and Urban Planning, Marche Polytechnic University, Via Brecce Bianche, Ancona 60131, Italy*
[k] *Department of Chemistry, The University of Hong Kong, Pokfulam Road, Hong Kong, China*
[l] *Hong Kong Quantum AI Lab, 17 Science Park West Avenue, Hong Kong, China*
[m] *Chemistry Department, Sapienza University of Rome, P. A. Moro 5, Rome 00185, Italy*

ARTICLE INFO

ABSTRACT

Understanding of interfacial Li$^+$ solvation shell structures and dynamic evolution at the electrode/electrolyte interface is requisite for developing high-energy-density Li batteries. Herein, the reorganization of Li$^+$ solvation shell at the sulfur/electrolyte interface along with the presence of a trace amount of lithium polysulfides is verified by *in-situ* sum frequency generation (SFG) spectroscopy together with density functional theory (DFT) calculations. Both the spectroelectrochemical and DFT calculation results reveal a strongly competitive anion adsorption of the polysulfide anion additive against the pristine electrolyte anion on the sulfur cathode surface, reorganizing the interfacial local solvation shell structure facilitating rapid Li ion transfer and conduction. Meanwhile, the evolution of the SFG signals along with the discharging/charging cycle exhibits improved reversibility, indicating the transformation of the inner Helmholtz plane layer into a stable molecular-layer polysulfide interphase rather than a dynamic diffusion layer. Consequently, applications in practical Li-S batteries reveal the capacity and cycling stability of the corresponding cells are significantly enhanced. Our work provides a methodology using *in-situ* SFG for probing solvation reorganization of charge carriers at electrochemical interfaces.

1. Introduction

Probing and understanding the chemical surroundings of the electrode/electrolyte interface such as solvation shell structure and dynamic evolution under an *in-situ/operando* practical working condition is the "Holy Grail" for investigations of electrochemical battery systems at the molecular level [1–8]. In contrast to intercalation-type lithium-ion batteries (LIBs), the representative conversion-based lithium-sulfur

---

(Li-S) batteries have garnered increasing attention owing to their high theoretical energy density (2600 Wh kg^{-1}) [4,9–12]. Currently, Li-S batteries are hampered by the issues of polysulfide shuttling, sluggish reaction kinetics, and the growth of Li dendrite [12–14]. The multi-step conversion reactions of sulfur involve a series of exchanges of Li$^+$ between electrolyte and electrode, which must overcome the energy barriers against the solvation/desolvation and diffusion of the charge carriers. Such barriers partially contribute to the sluggish conversion kinetics and the consequent accumulation and shuttling loss of polysulfide intermediates [15–17]. Thus, a detailed understanding of Li$^+$ solvation shell structure and dynamic behaviors at the electrode/electrolyte interface is necessary to resolve the critical challenges of Li-S batteries [18–24].

Recently, the crowded solvation shell by adding suitable electrolyte additives or electrochemical catalysts to dissociate Li$^+$-solvents complex were achieved to accelerate desolvation behaviors at the interface, indicating the profound effects of Li ion solvation on reaction kinetics [15,25–28]. Till now, advanced *in-situ* microscopy and spectroscopy tools, e.g. *in-situ* scanning electron microscopy (SEM), transmission electron microscopy (TEM), X-ray adsorption spectroscopy (XAS) and Raman spectroscopy, have been employed to characterize Li-ion or Li-S batteries, providing meaningful information regarding the conversion kinetics and the degradation mechanisms [2,3,16,29–35]. However, most of the *in-situ/operando* studies are focused on either monitoring physical/chemical changes in the state of sulfur or detecting and tracking the shuttling phenomena, which depends on the depth of penetration and the bulk contributions of signal [2,31,33]. The utilization efficiency and cycling stability of sulfur cathodes strongly rely on the kinetics of releasing free Li ions from their solvation shell at the interface, costing extra energy during the transfer of Li$^+$ across the interface [15]. Furthermore, since the charge/discharge current rate of a battery is often dominated by the interfacial ion transfer kinetics, understanding the effect of the local surroundings at the electrode/electrolyte interface in relation to the Li$^+$ solvation/desolvation processes is important for designing battery systems with high-rate performance [10–12,16,19,36,37]. Therefore, it is of significance to monitor the structure evolution and dynamics in real-time at the molecular level, particularly the variation of the solvation shell structure in the electrode/electrolyte interface region of a practical working battery [1,38]. Thus far, effective *in-situ/operando* methods to selectively probe the interfacial molecular information of lithium batteries remain limited.

Sum frequency generation (SFG) spectroscopy with inherent interfacial selectivity and sensitivity has demonstrated utility for *in-situ* investigations of LIBs and electrocatalysis systems [39–47]. However, current *in-situ* SFG researches on LIBs are based on model-designed battery configurations, which are not representative of operational practical cells (Fig. S1) [41–44,48–50]. Selectively investigating the Li$^+$ solvation shell structure and its dynamic variations in the interface region is limited by problems of low signal/noise ratio and high interference from the bulk solution. For similar reasons, the interfacial chemistry of solvation behaviors in Li-S cells by *in-situ* SFG technique has yet to be studied. In this work, density functional theory (DFT) calculations and experimental characterizations are combined through *in-situ* SFG electrochemical cell, revealing new insights on the polysulfide-based anion adsorption layer as well as the reorganization of Li$^+$ solvation shell structure at the interface. Firstly, the *in-situ/operando* SFG results suggest an evident fluctuation in the adsorption of electrolyte anions (TFSI$^-$) at the cathode interface with irreversible circulation in the control sample. Whereas much weaker anion adsorption with less variation and high cycling reversibility is observed after the introduction of a trace amount of polysulfide anion additive, indicating the dominantly adsorbed polysulfide molecules change the local chemical surrounding in Li$^+$ solvation shell structure and the constituent(s) of the inner Helmholtz plane. The well-correlated electrochemical improvements of the corresponding cells with lower interfacial resistance and

decreased charging overpotential indicate that the reorganization of solvation shell facilitates the exchanging of Li$^+$ between the sulfur cathode and the electrolyte by decreasing the interfacial desolvation/solvation energy barriers, as confirmed by DFT calculations. In the practical cell, the optimized solvation shell structure is also beneficial for forming the Li$^+$ diffusion-accelerated electrode/electrolyte interphase, thus improving the cycling reversibility and stability of the sulfur cathode. This work provides a use-case for SFG as a tool to study the interfacial reorganization of solvation shell(s) and for the modulation of the cathode/electrolyte interface to elevate the performances of Li-S cells.

2. Experimental section

2.1. Fabrication of sulfur and lithium sulfide electrodes

Graphene oxide (GO), nitrogen-doped graphene (NG), oxidative carbon nanotube (OCNT) and nitrogen-doped carbon nanotube (NCNT) were synthesized according to previous reports [36,51]. NG-NCNT@PANI nanocomposites were synthesized and the main difference is that the mass ratio of NCNT and NG powders is equal to 3:1 (200 mg in total) according to previously published reports [36]. The S@NG and Li$_2$S@NC nanocomposites were made by the same method according to previous literatures [19,52].

2.2. Preparation of polysulfides solution

Commercial sulfur (448 mg) and commercial Li$_2$S (92 mg) were added into 10 mL mixed solvents (DOL/DME, 1:1, by volume). After continuously stirring for 12 h, the homogeneous Li$_2$S$_8$ solution (0.2 mol L^{-1}) was obtained at 60 °C. A proper amount volume of as-prepared homogenous Li$_2$S$_8$ solution was added in 20 mL of pristine electrolyte (1 mol L^{-1} LiTFSI dissolved in DME/DOL) to form different concentrations of 0.1 mmol L^{-1} (0.1 mM) and 0.25 mmol L^{-1} (0.25 mM) Li$_2$S$_8$ in pristine electrolyte, respectively.

2.3. Fabrication of Li-S coin cells and in-situ SFG cell

The prepared sulfur electrode was fabricated by coating the slurry on the Al current collector (Thickness: 16 μm) and then compressed under pressure, yielding a relatively smooth electrode surface with a certain extent of mirror reflection rather than random scattering. The *in-situ* SFG cell based on sulfur cathode was prepared by using Whatman fiberglass (260 μm) filter as the separator and lithium metal foil as the anode. The electrolyte is composed of 1 mol L^{-1} LiTFSI in DME/DOL (1:1, by volume) with or without Li$_2$S$_8$ additive. For the purpose of demonstrating the functions in real Li-S batteries, optimized routine electrolyte (1 mol L^{-1} LiTFSI dissolved in DME/DOL with 1 wt.% LiNO$_3$) or with pre-added Li$_2$S$_8$ electrolyte and Celgard 2400 were used for the assembly of coin cells for sulfur electrodes or Li$_2$S electrodes.

2.4. Material and device characterizations

Field-emission scanning electron microscopy (Hitachi S4800) was applied to observe the surface morphological structure of different cycled sulfur cathodes. Land CT2001 automatic battery test systems was selected to measure the electrochemical cycling behaviors of sulfur or Li$_2$S cathode. Cyclic voltammetry of the sulfur cathode was carried out on a VMP-3 electrochemical station at 0.025 mV s^{-1}. The electrochemical impedance spectroscopy of *in-situ* SFG cell was carried out from 200 kHz to 100 mHz at open-circuit voltage.

3. Results and discussion

Before visualizing practical interface information, the *in-situ* cell configuration of the SFG spectroelectrochemical cell is illustrated in
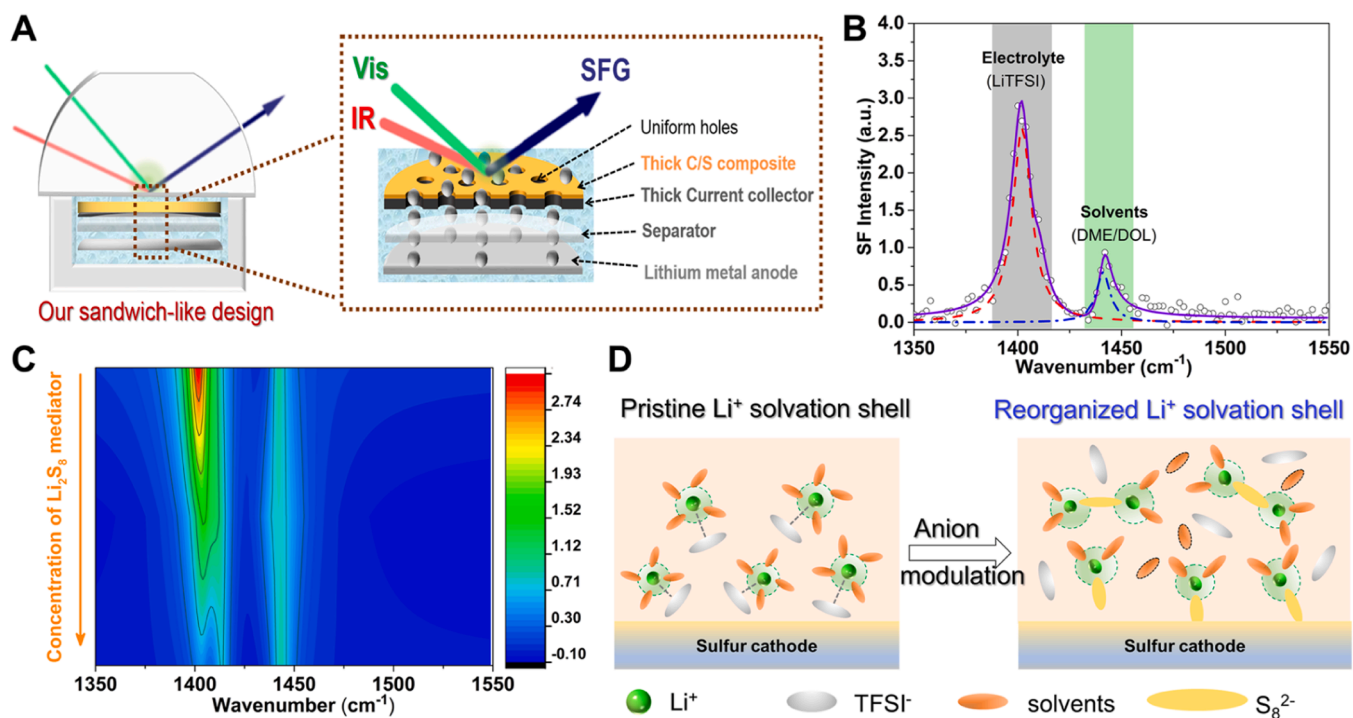
Fig. 1. (A) Schematic illustration of our *in-situ* SFG electrochemical cell with the hole-plate electrode configuration similar to real working condition. (B) The *ssp*-polarization SFG spectrum from the surface of S@NG cathode in a typical electrolyte (1 mol L^{-1} LiTFSI in 1:1 DME/DOL). The fitted peaks (the red dashed line and the blue dash-dot line) can be assigned to the adsorbed LiTFSI and DME/DOL, respectively. **(C)** SFG spectra of the cathode/electrolyte interface in the presence of different concentration of pre-added Li$_2$S$_8$ mediator at the open-circuit voltage (OCV) state. (D) The schematic illustration of the reorganization behaviors of Li$^+$ solvation shell after introducing the polysulfide anion at the sulfur/electrode interface.

Fig. 1A, which makes the electrode/electrolyte interface accessible to the probing lights while operating in a condition closer to the practical cells. To ensure sufficient electrolyte penetration for smooth Li$^+$ transfer for later charge/discharge, numerous holes (~500 μm) are uniformly punched on the cathode. The signal of SFG results from the electrode/electrolyte interface by fixing the distance between the CaF$_2$ window and the electrode plane. As confirmed by cyclic voltammetry (CV) and electrochemical impedance spectroscopy (EIS), the as-fabricated *in-situ* SFG cell operates efficiently as a Li-S coin cell without retarding of ion transport (Fig. S2), guaranteeing the occurrence of redox processes [9, 51,53–57]. Initially, the pristine electrolyte (PE, 1 mol L^{-1} LiTFSI in DOL/DME (1:1, v:v)) is subjected to SFG measurements to clarify the contribution of the different species. By comparing each of the constituents in the PE electrolyte (Fig. S3), the strong and sharp peak at ~1402 cm^{-1} and the shoulder at ~1410 cm^{-1} is assigned to the adsorbed LiTFSI electrolyte salt (Fig. 1B), most likely due to the out-of-plane and in-plane asymmetric stretching of S=O in the TFSI$^-$, respectively [58–64]. As calculated, the energy of the S=O bond increases as LiTFSI is adsorbed onto the nitrogen-doped graphene-based electrode, which explains the blue shift of its vibrational frequency [59–61]. The relatively weak and broad peak at ~1440 cm^{-1} can be readily assigned to the solvent molecules (DME/DOL) [37,65]. Also, the negligible changes at ~1440 cm^{-1} and the asymmetrical torsion vibration mode of the methylene (-CH$_2$-) group belong to solvent molecule adsorption at subsequent discharge/charge states (Fig. S4). Therefore, the solvent peak at ~1440 cm^{-1} can serve as an internal standard signal to quantitatively evaluate the anion adsorption and the reorganization of solvation shell structure by anion modulation. Here, the intensity ratio of the TFSI$^-$ peak (~1402 cm^{-1}) to the solvent peak (~1440 cm^{-1}) as I_E/I_S (E for electrolyte and S for solvent, respectively) is defined, monitoring the surface evolution of anion-related solvation shell structure. Since an SFG peak intensity is proportional to the square of the surface number density of the related species [40,43,44], the square root of I_E/I_S, i.e. $(I_E/I_S)^{0.5}$, is used as an

index to observe changes in the solvation surrounding of interfacial TSFI$^-$ species.

The static TFSI$^-$ anion adsorption on the electrode with/without Li$_2$S$_8$ are monitored at the interface under open-circuit voltage (OCV) state. Without the Li$_2$S$_8$, a rich amount of TFSI$^-$ anions is adsorbed (Fig. 1C). With the introduction of lithium polysulfide mediator of Li$_2$S$_8$ (LPSM) in the PE (denoted as PE+LPSM), the adsorption behaviors and $(I_E/I_S)^{0.5}$ of TFSI$^-$ show the reverse trend with sharply decreasing SF intensity (Figs. 1C and S5), indicating the changes of the related solvation shell structure with more Li$_2$S$_8$ coordination. For example, under 0.25 mmol L^{-1}, the $(I_E/I_S)^{0.5}$ value decreases by ~6.6 times (from 2.7 to 0.41), corresponding to approximately 85 % desorption of the initially adsorbed TFSI$^-$ species from the interfacial solvation shell. All the fitting parameters for the SFG spectra were summarized in Table S1. As illustrated in Fig. 1D, the pristine TFSI$^-$ anion-dominated Li ion solvation shell is altered and tends to be replaced by polysulfide anion under the presence of the Li$_2$S$_8$ mediator [37], forming a greater proportion of polysulfide-decorated aggregates or coordinate ion pairs. Subsequently, the optimal polysulfide-assisted Li$^+$ solvation structure turned into a preferentially adsorbed molecular layer on the cathode surface by repelling off the initially adsorbed TFSI$^-$.

To ascertain the Li$^+$ solvation shell dynamic evolution during the charging/discharging process, the evolutions of SFG spectra were recorded. In the PE, the initial value of $(I_E/I_S)^{0.5}$ is ~2.7 at the OCV state and it decreases to 2.3 upon being discharged to 2.3 V (Li$_2$S$_4$ discharge product), and then starts to increase and reaches 4.1 (Li$_2$S discharge product) at the fully discharged state. When recharged, the $(I_E/I_S)^{0.5}$ reverses its variation trend (from 4.1 to 1.4, and then to 1.7); but it does not fully recover to its initial value (1.7 *vs.* 2.7). However, with LPSM (Figs. 2B and S6), the $(I_E/I_S)^{0.5}$ value experiences a similar decreasing then increasing trend during the discharge process (from 0.41 to 0.33, and then to 0.67 at the fully discharged state), whereas the subsequent recharge process shows a complete reversal of the values (from 0.67 to
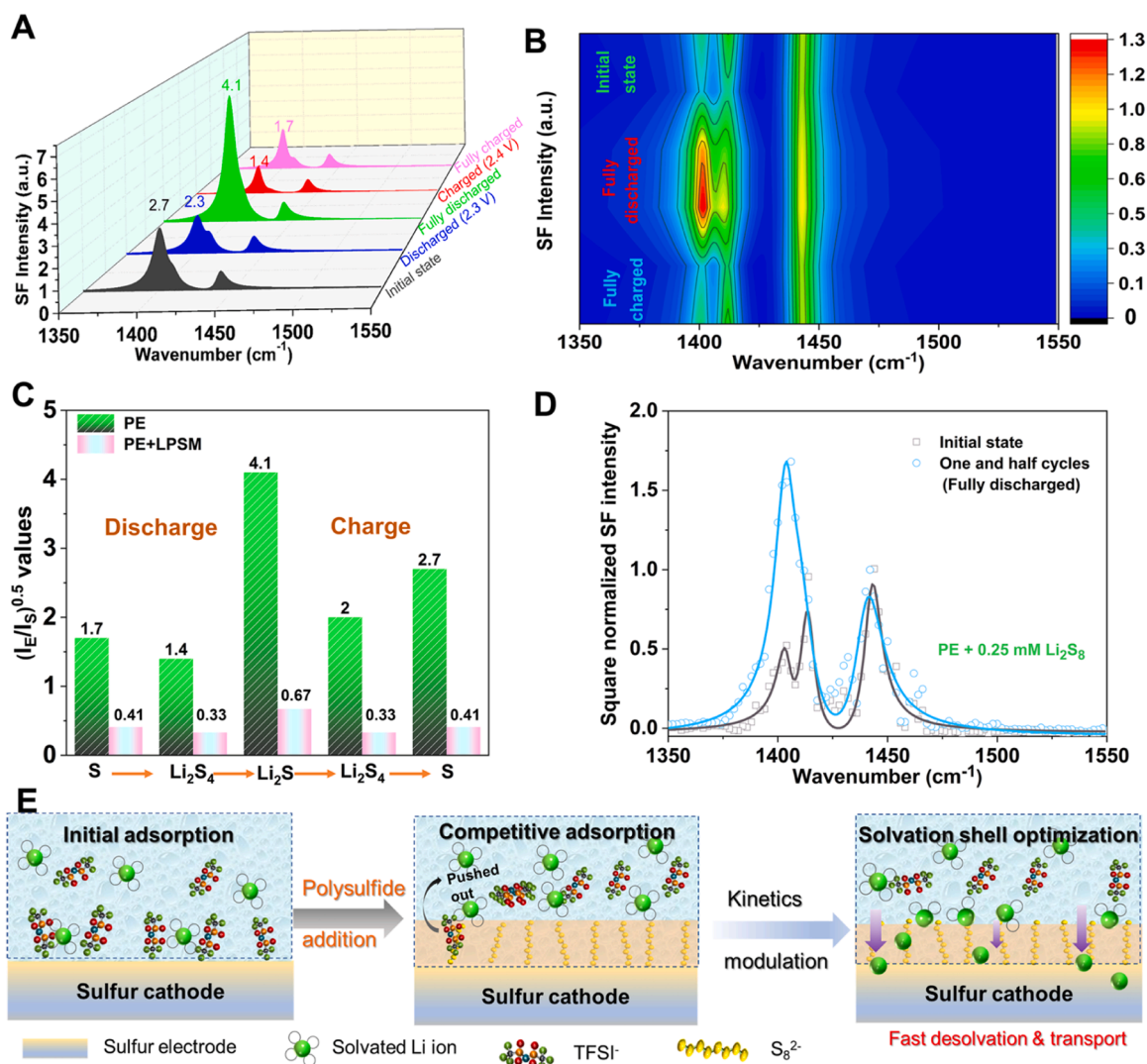
Fig. 2. *In-situ* SFG spectra of the S@NG cathode/electrolyte interface in (A) pristine electrolyte; (B) with 0.25 mmol L^{-1} polysulfide additive in the electrolyte at different charge/discharge depths. (C) Comparison of the $(I_E/I_S)^{0.5}$ values without and with pre-added Li$_2$S$_8$ at different electrochemical states. (D) The SFG spectrum of the *in-situ* cell with reorganized solvation shell after one and half cycles. (E) Schematic illustration of dynamic competitive adsorption between polysulfide and LiTFSI on the cathode and the formed optimal solvation shell on accelerating ion transport across the interface for superior redox kinetics.

0.33, and then to 0.41 at the fully recharged state). As summarized in Fig. 2C, the interfacial adsorption amount of TFSI$^-$ was significantly decreased in the presence of LPSM, which holds true not only at the initial OCV state but also at each discharging or charging state. For PE, the value of $(I_E/I_S)^{0.5}$ varies and experiences a fluctuation amplitude up to 2.7 (Fig. 2C). For the cell with optimal Li$^+$ solvation shell, the $(I_E/I_S)^{0.5}$ value varies in a much narrower range from 0.33 to 0.67, with a fluctuation amplitude of only 0.34. The reversibility of the $(I_E/I_S)^{0.5}$ value implies the reversible amount of TFSI$^-$ species and the reversible reorganization of the optimal Li$^+$ solvation shell structure in the dynamic electrochemical processes, demonstrating the reversibility of the polysulfide-assisted solvation shell in various states. Meanwhile, the different polarization configuration of the SFG with *ppp* polarization was also conducted. Surprisingly, the SFG spectra at *ppp* configuration were almost identical to those at *ssp* (Fig. S7), indicating the SFG response is independent of the polarization of the incident light. Compared with the initial SFG spectrum at OCV state, the TFSI$^-$ signal is enhanced but still maintains a low level at fully discharged state of the second cycle (Fig. 2D), indicating the feasibility of reorganized solvation shell structure for fast Li ion transport in the later cycles. These results display the main difference in SFG behavior between the pre-added Li$_2$S$_x$ and

the *in-situ* generated ones in the electrolyte. The Li$^+$ solvation structure in the inner Helmholtz plane layer is strongly related to the local distribution of Li$_2$S$_x$ and would vary for the different sites in the self-generated one. On the other hand, the adsorption of the pre-dissolved Li$_2$S$_x$ additives in the ether-based electrolyte is much more uniform at the interface. This is the main reason why the sulfur cathodes behave differently with/without polysulfide additives in the electrolyte when assembling cells. The full process and functions of LPSM are illustrated in Fig. 2E: (1) the polysulfide (Li$_2$S$_8$) molecules strongly compete with the LiTFSI at the interface, reorganizing the solvation shell structure and forming a sulfurophilic mediator layer on the cathode surface; and (2) with the polysulfide inner Helmholtz layer, fast desolvation behaviors from Li$^+$ solvation shell are realized for the facilitated insertion/extraction of the cathode (S or Li$_2$S), decreasing the interfacial barriers for fast lithium-ion transfer with the formation of a potential buffer layer [34,47,66].

To elucidate the reorganized Li$^+$ solvation shell, DFT calculations were performed. Firstly, the competitive adsorption between Li$_2$S$_8$ and LiTFSI was imitated, and the results display that Li$_2$S$_8$ possesses a much higher binding energy on the electrode surface than LiTFSI (Figs. 3A and S8). According to the Gibbs-Helmholtz equation $\Delta G = -RT\ln K$ the
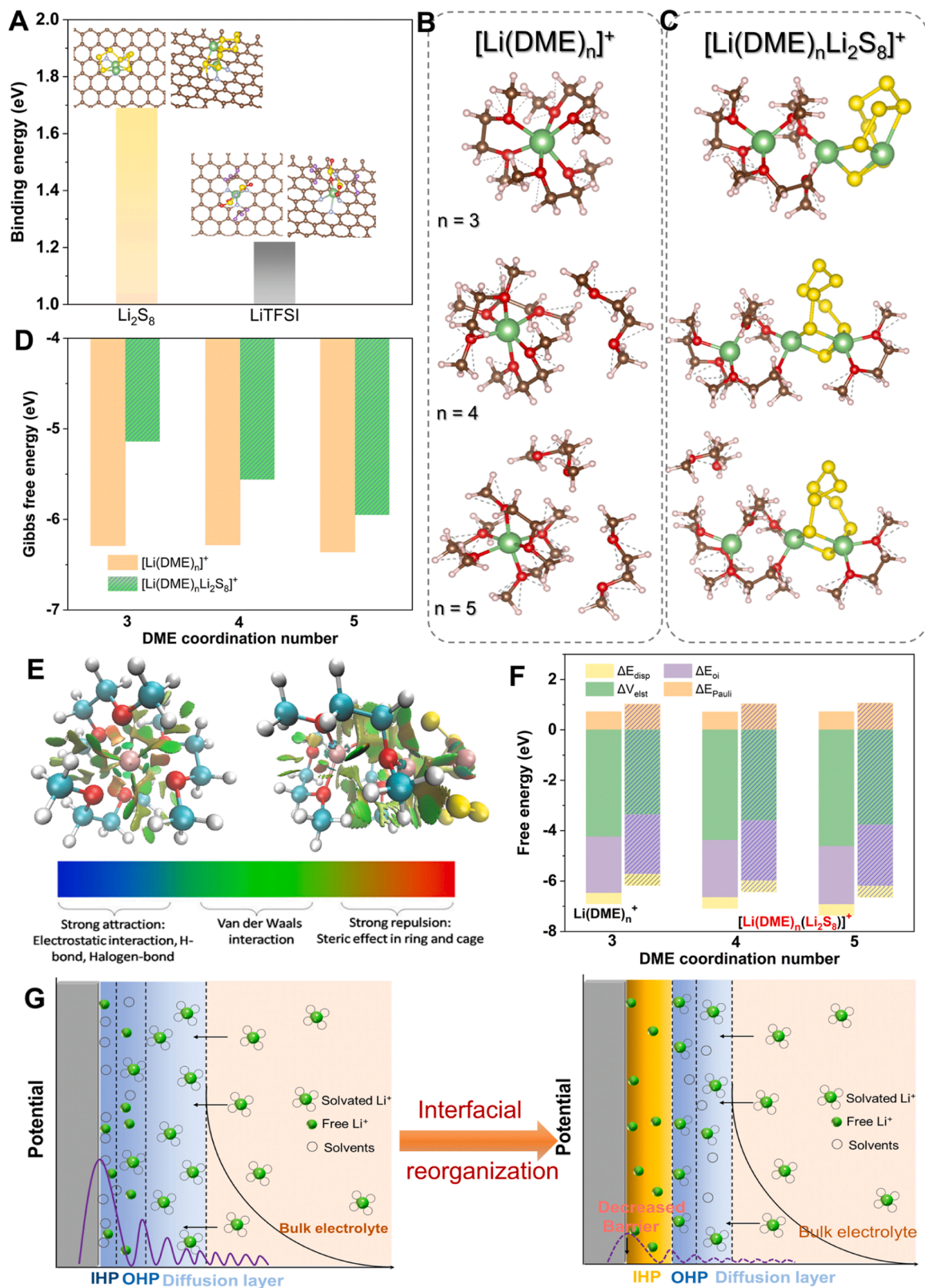
Fig. 3. (A) Comparison of the binding energies of Li_2S_8 and LiTFSI on graphene and NG, respectively. Various optimized structures of representative (B) $[Li(DME)_n]^+$ and (C) $[Li(Li_2S_8)(DME)_n]^+$ complexes (n = 3,4,5). (D) Comparison and summary of the solvation Gibbs free energy of $[Li(DME)_n]^+$ and $[Li(Li_2S_8)(DME)_n]^+$ complexes with different DME coordination number. (E) The 3D isosurface view of reduced density gradient (RDG), The isovalue is set to 0.5 a.u. The color represents the sign $(\lambda 2)\rho$. (F) Comparisons of components in the energy decomposition analysis of the $[Li(DME)_n]^+$ and $[Li(Li_2S_8)(DME)_n]^+$ complexes with different DME coordination numbers. The brown, yellow, red, light-green, light-blue, and light-purple balls represent carbon, sulfur, oxygen, lithium, nitrogen, and fluorine atoms, respectively. (G) The evolution of the double layer near the cathode before and after the polysulfide modulation, changing the inner Helmholtz plane.

corresponding difference in their adsorption coefficient on the surface can be roughly estimated as high as several orders of magnitude, which explains why a small amount of polysulfides is capable of resulting in a substantial desorption of TSFI$^-$ species from the cathode/electrolyte interface. Further, the Li$^+$ solvation behaviors in the anion-abundant and solvent-rich environments are simulated. As shown in Fig. 3B, various [Li(DME)$_n$]$^+$ cluster structures were initially optimized and the representative structures were selected from low-lying isomers. In the typical [Li(DME)$_3$]$^+$ solvation structure, oxygen atoms in the DME were coordinated with the central Li$^+$ and the bond length between central Li$^+$ and coordinated oxygen atom was ~2.15 Å (Table S2). Increasing the number of explicit solvent molecules in the [Li(DME)$_n$]$^+$, three adsorbed DME molecules were still retained in the first inner solvation shell while a greater proportion of other DME molecules were adsorbed outside the first solvation shell (Fig. 3C), slightly affecting the Li-O distance between the central Li$^+$ and DME molecules in the first solvation shell (Table S2). However, incorporating Li$_2$S$_8$ into the [Li(DME)$_3$]$^+$ system, the solvation free energy of Li$^+$ in the [Li(Li$_2$S$_8$)(DME)$_n$]$^+$ was slightly increased, implying the likelihood for further decomposition and desolvation. This is attributed to the extra Li atom in the Li$_2$S$_8$ molecule which can disrupt the initial solvation shell by forming a Li-O pair between Li$_2$S$_8$ and inner DME, replacing the inner oxygen coordination site with Li$_2$S$_8$ additive. These results indicate that it is mainly the Li$^+$ in the Li$_2$S$_8$ molecule that affects the solvation shell structure, not the polysulfide chain. It suggests all the other types of soluble lithium polysulfides should behave similarly to the Li$_2$S$_8$ additives. The longer chain of S$_8^{2-}$ causes the molecules in the adsorption layer to align in an ordered manner along a preferential orientation, which would further benefit the Li$^+$ transport and exchange. Meanwhile, the coordination number of central Li$^+$ decreased to 4, less than the original six coordination number. For the other [Li(DME)$_4$]$^+$ and [Li(DME)$_5$]$^+$ systems, a similar reduction of coordination number was observed for the central Li$^+$, indicating the decrease of solvation energy. These geometric structures indicate that the Li$_2$S$_8$ could strongly affect the first solvation shell, reducing the interaction strength between the central Li$^+$ and its neighboring solvent molecules i.e., DME. Successively, the desolvation energies of the [Li(DME)$_n$]$^+$ with/without Li$_2$S$_8$ were compared. As summarized in Fig. 3D, all the [Li(DME)$_n$]$^+$ solvation shell structures exhibit Gibbs free energies of ~6.3 eV. However, with the introduction of Li$_2$S$_8$, the Gibbs free energies of the [Li(DME)$_n$]$^+$ were decreased by ~0.4–1.1 eV. Dissociating Li$^+$ from the [Li(Li$_2$S$_8$)(DME)$_n$]$^+$ system would reduce the energy by ~20–27 kJ mol^{-1}, demonstrating the benefit of Li$_2$S$_8$ in reorganizing the first inner solvation shell for fast Li$^+$ desolvation. Figs. 3E and S9 display there only exist Van der Waals interactions in the [Li(DME)$_n$]$^+$ systems while the other two oxygen atoms in the shell layer were coordinated to the Li$^+$ in the Li$_2$S$_8$ molecule. It is reasonable to conclude that the Li$_2$S$_8$ molecule modulates the central Li$^+$ solvation shell structure, which could reduce its desolvation energy and change the original solvation shell structure of [Li(DME)$_n$]$^+$ into [Li(Li$_2$S$_8$)(DME)$_n$]$^+$. Furthermore, to achieve a comprehensive understanding of the reduction of solvation energy by introducing Li$_2$S$_8$, energy decomposition analysis was performed for solvation species without or with the Li$_2$S$_8$ molecule. Three components of the interaction energy, i.e., the orbital interaction energy ΔE_{oi}, the Pauli repulsion ΔE_{Pauli}, and the dispersion energy ΔE_{disp} were almost the same though changing different numbers of DME in the solvation shell structure (Fig. 3F). However, the electrostatic interaction $\Delta V_{electrostatic}$ exhibits the significance to stabilize the solvation structure than the orbital interaction and the dispersion. Compared with the same coordination number in the [Li(DME)$_n$]$^+$, the presence of the Li$_2$S$_8$ molecule is capable of reducing the strength of the electrostatic interaction by 0.74–0.84 eV. These computational results demonstrate that the Li$_2$S$_8$ helps to decrease the intrinsic electrostatic interaction of the [Li(DME)$_n$]$^+$, which is responsible for the reduction in desolvation energy for releasing free Li ions. Fig. 3G depicts the variation of the double layer at the electrode/electrolyte interface. In the PE, the adsorbed solvents accompanied with

TFSI$^-$ anions fill in the inner Helmholtz plane (IHP) layer. However, after introducing polysulfide anion in modulating Li$^+$ solvation shell structure, the polysulfide layer dominates the IHP layer, providing the path with decreased barriers for Li ion transport across the interface.

To validate the superiority of optimized solvation shell structure for fast Li$^+$diffusion in practical battery devices, the electrochemical performances of Li-S (S and Li$_2$S cathodes) cells were compared. As expected, the cell with optimal solvation shell shows improved initial capacity and cycling stability than that without Li$_2$S$_8$ mediator. As shown in Fig. 4A, the sulfur cathode exhibits an initial discharge specific capacity of 932 mA h g^{-1} at 1 C (1 C = 1675 mA g^{-1}, based on S) in LPSM-decorated electrolyte, much higher than the cathode without solvation shell reorganization. After 80 cycles, the sulfur cathode still maintains a high capacity of 839 mA h g^{-1}, in contrast to 665 mA h g^{-1} of the pristine cathode with PE. After cycling, the scanning electron microscope (SEM) images of the S@NG cathode with/without solvation reorganization were conducted. Both SEM images exhibit a smooth surface and a uniform distribution of the sulfur species without any sulfur or Li$_2$S aggregation at fully charged/discharged states (Figs. 4B and S10), verifying the superior solvation shell reorganization by polysulfide mediator on modulating interfacial Li$^+$ transport and accelerating electrochemical reactions. In the Li-Li$_2$S cells, the decomposition barrier of Li$_2$S is determined by the Li ion diffusion across the Li$_2$S/electrolyte interface and solvation shell. Figs. 4C and S11 show the initial charge/discharge curves at 0.05 C (1 C = 1166 mA g^{-1}, based on Li$_2$S) up to an initial cut-off voltage of up to 3.5 V [67]. With the reorganized solvation shell, the delithiation barrier of Li$_2$S can be significantly reduced from 3.12 V to 2.88 V. The higher potential barrier of pristine Li$_2$S suggests more resistance to lithium ion transport while a more efficient lithium-ion exchange is obtained through the polysulfide mediator layer [68,69]. This agrees well with the role of the polysulfide mediator which changes the solvation shell structure, buffers the drastic change of binding environment for Li$^+$ from Li$_2$S to the electrolyte and diminishes the extra interfacial energy barrier caused by the adsorption/desorption of TFSI$^-$ during Li$^+$ transfer (Fig. 2E). Fig. 4D also shows that the polysulfide mediator in the battery system can significantly improve the capacity and stability of Li-Li$_2$S cells.

4. Conclusion

In summary, the dynamic behaviors of Li$^+$ solvation shell structure against Li$_2$S$_8$ anion competitive adsorption are comprehensively investigated using *in-situ* interface-sensitive SFG spectroscopy and DFT calculations. The results show that the polysulfide-assisted Li$^+$ solvation structure has a much higher affinity to the electrode surface than TFSI$^-$-assisted ones at the electrode/electrolyte interface, thus reorganizing the Li$^+$ solvation shell structure in the interfacial vicinity. With the optimal Li$^+$ solvation shell, the desolvation governed interfacial lithium-ion transfer barriers are significantly reduced, endowing the Li-S cells with superior reversibility and capacity at high current rates. This study provides key insights into the solvation shell structure and the role of a trace amount of polysulfides in Li-S battery, establishing a practical *in-situ* SFG methodology for probing energy storage systems.

CRediT authorship contribution statement

Jian Wang: Conceptualization, Methodology, Resources, Writing – original draft, Writing – review & editing. **Haitao Liu:** Investigation, Methodology, Resources, Writing – original draft, Writing – review & editing. **Jing Zhang:** Investigation, Methodology, Writing – review & editing. **Qingbo Xiao:** Investigation, Writing – review & editing. **Chong Wang:** Investigation, Writing – review & editing. **Yongzheng Zhang:** Investigation, Writing – review & editing. **Meinan Liu:** Investigation, Writing – review & editing. **Qi Kang:** Investigation, Writing – review & editing. **Lujie Jia:** Investigation, Writing – review & editing. **Dong Wang:** Investigation, Writing – review & editing. **Qi Li:** Investigation,
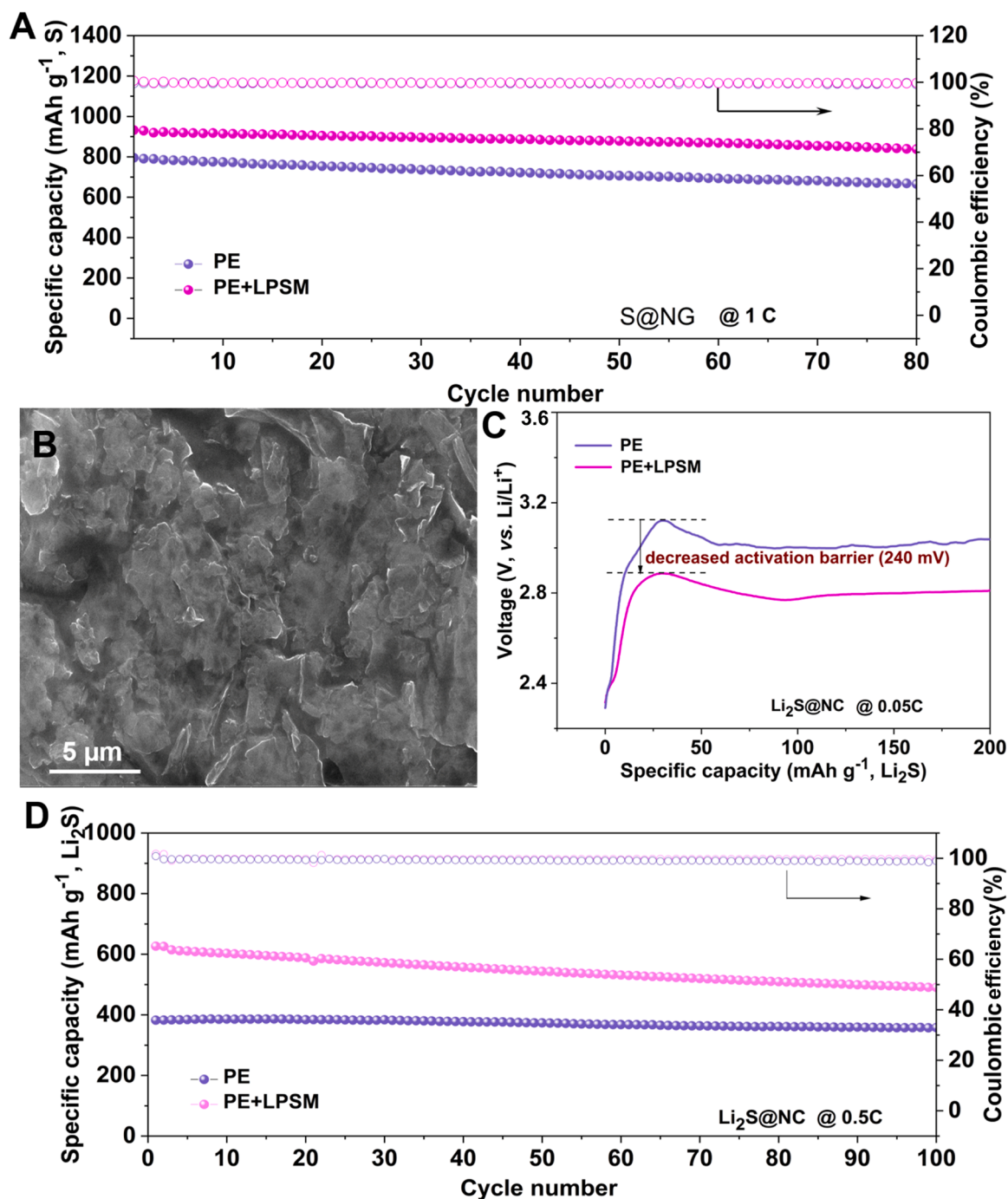
Fig. 4. (A) Comparison of cycling performance for S@NG cathodes with and without polysulfide mediator at 1 C. (B) SEM image of a cycled sulfur cathode in fully discharged state under polysulfide-modulated solvation shell. (C) Comparison of activation barriers for Li$_2$S@NC cathodes with and without polysulfide mediator. (D) Comparison of cycling performance at 0.5 C for Li$_2$S@NC cathodes with and without polysulfide mediator.

Writing – review & editing. **Wenhui Duan:** Investigation, Methodology, Resources, Writing – review & editing. **Henry Adenusi:** Resources, Writing – review & editing. **Stefano Passerini:** Conceptualization, Funding acquisition, Methodology, Resources, Supervision, Writing – original draft, Writing – review & editing. **Yuegang Zhang:** Conceptualization, Funding acquisition, Methodology, Resources, Supervision, Writing – original draft, Writing – review & editing. **Hongzhen Lin:** Conceptualization, Funding acquisition, Methodology, Resources, Supervision, Writing – original draft, Writing – review & editing.

Declaration of competing interest

The authors declare that they have no known competing financial interests or personal relationships that could have appeared to influence the work reported in this paper.

Data availability

Data will be made available on request.

Acknowledgments

Supplementary materials

Supplementary material associated with this article can be found, in the online version, at doi:10.1016/j.ensm.2024.103289.

References

[1] X. Yu, A. Manthiram, Electrode-Electrolyte Interfaces in Lithium-Sulfur Batteries with Liquid or Inorganic Solid Electrolytes, Acc. Chem. Res. 50 (2017) 2653–2660.

[2] H.L. Wu, L.A. Huff, A.A. Gewirth, In situ Raman spectroscopy of sulfur speciation in lithium-sulfur batteries, ACS Appl. Mater. Interfaces 7 (2015) 1709–1719.

[3] J. Tan, D. Liu, X. Xu, L. Mai, In situ/operando characterization techniques for rechargeable lithium-sulfur batteries: a review, Nanoscale 9 (2017) 19001–19016.

[4] J. Wang, J. Yang, Q. Xiao, J. Zhang, T. Li, L. Jia, Z. Wang, S. Cheng, L. Li, M. Liu, H. Liu, H. Lin, Y. Zhang, In Situ Self-Assembly of Ordered Organic/Inorganic Dual-Layered Interphase for Achieving Long-Life Dendrite-Free Li Metal Anodes in LiFSI-Based Electrolyte, Adv. Funct. Mater. 31 (2021) 2007434.

[5] J. Ryu, M. Park, J. Cho, Advanced Technologies for High-Energy Aluminum-Air Batteries, Adv. Mater. 31 (2019) e1804784.

[6] J. Wang, J. Zhang, S. Duan, L. Jia, Q. Xiao, H. Liu, H. Hu, S. Cheng, Z. Zhang, L. Li, W. Duan, Y. Zhang, H. Lin, Lithium Atom Surface Diffusion and Delocalized Deposition Propelled by Atomic Metal Catalyst toward Ultrahigh-Capacity Dendrite-Free Lithium Anode, Nano Lett. 22 (2022) 8008–8017.

[7] X. He, D. Bresser, S. Passerini, F. Baakes, U. Krewer, J. Lopez, C.T. Mallia, Y. Shao-Horn, I. Cekic-Laskovic, S. Wiemers-Meyer, F.A. Soto, V. Ponce, J.M. Seminario, P. B. Balbuena, H. Jia, W. Xu, Y. Xu, C. Wang, B. Horstmann, R. Amine, C.C. Su, J. Shi, K. Amine, M. Winter, A. Latz, R. Kostecki, The passivity of lithium electrodes in liquid electrolytes for secondary batteries, Nat. Rev. Mater. 6 (2021) 1036–1052.

[8] J. Wang, J. Zhang, J. Wu, M. Huang, L. Jia, L. Li, Y. Zhang, H. Hu, F. Liu, Q. Guan, M. Liu, H. Adenusi, H. Lin, S. Passerini, Interfacial "Single-Atom-in-Defects" Catalysts Accelerating Li⁺ Desolvation Kinetics for Long-lifespan Lithium Metal Batteries, Adv. Mater. 35 (2023) 2302828.

[9] P.G. Bruce, S.A. Freunberger, L.J. Hardwick, J.M. Tarascon, Li-O₂ and Li-S batteries with high energy storage, Nat. Mater. 11 (2012) 19–29.

[10] J. Wang, J. Zhang, S. Cheng, J. Yang, Y. Xi, X. Hou, Q. Xiao, H. Lin, Long-Life Dendrite-Free Lithium Metal Electrode Achieved by Constructing a Single Metal Atom Anchored in a Diffusion Modulator Layer, Nano Lett. 21 (2021) 3245–3253.

[11] J. Wang, L. Jia, S. Duan, H. Liu, Q. Xiao, T. Li, H. Fan, K. Feng, J. Yang, Q. Wang, M. Liu, J. Zhong, W. Duan, H. Lin, Y. Zhang, Single atomic cobalt catalyst significantly accelerates lithium ion diffusion in high mass loading Li₂S cathode, Energy Storage Mater. 28 (2020) 375–382.

[12] J. Zhang, C. You, H. Lin, J. Wang, Electrochemical Kinetic Modulators in Lithium–Sulfur Batteries: From Defect-Rich Catalysts to Single Atomic Catalysts, Energy Environ. Mater. 5 (2022) 731–750.

[13] G. Zhou, H. Chen, Y. Cui, Formulating energy density for designing practical lithium–sulfur batteries, Nat. Energy 7 (2022) 312–319.

[14] J. Zhang, R. He, L. Jia, C. You, Y. Zhang, M. Liu, N. Tian, H. Lin, J. Wang, Strategies for Realizing Rechargeable High Volumetric Energy Density Conversion-Based Aluminum–Sulfur Batteries, Adv. Funct. Mater. 33 (2023) 2305674.

[15] L. Li, H. Tu, J. Wang, M. Wang, W. Li, X. Li, F. Ye, Q. Guan, F. Zhu, Y. Zhang, Y. Hu, C. Yan, H. Lin, M. Liu, Electrocatalytic MOF-Carbon Bridged Network Accelerates Li⁺-Solvents Desolvation for High Li⁺ Diffusion toward Rapid Sulfur Redox Kinetics, Adv. Funct. Mater. 33 (2023) 2212499.

[16] X. Li, Q. Guan, Z. Zhuang, Y. Zhang, Y. Lin, J. Wang, C. Shen, H. Lin, Y. Wang, L. Zhan, L. Ling, Ordered Mesoporous Carbon Grafted MXene Catalytic Heterostructure as Li-Ion Kinetic Pump toward High-Efficient Sulfur/Sulfide Conversions for Li-S Battery, ACS Nano 17 (2023) 1653–1662.

[17] S.Y. Wu, X. Li, Y.Z. Zhang, Q.H. Guan, J. Wang, C.Y. Shen, H.Z. Lin, J.T. Wang, Y. L. Wang, L. Zhan, L.C. Ling, Interface engineering of MXene-based heterostructures for lithium-sulfur batteries, Nano Res. 16 (2023) 9158–9178.

[18] M. Liu, F. Ye, W. Li, H. Li, Y. Zhang, Chemical routes toward long-lasting lithium/sulfur cells, Nano Res. 9 (2016) 94–116.

[19] J. Wang, L. Jia, J. Zhong, Q. Xiao, C. Wang, K. Zang, H. Liu, H. Zheng, J. Luo, J. Yang, H. Fan, W. Duan, Y. Wu, H. Lin, Y. Zhang, Single-atom catalyst boosts electrochemical conversion reactions in batteries, Energy Storage Mater. 18 (2019) 246–252.

[20] Y.X. Yin, S. Xin, Y.G. Guo, L.J. Wan, Lithium-sulfur batteries: electrochemistry, materials, and prospects, Angew. Chem. Int. Ed. Engl. 52 (2013) 13186–13200.

[21] J. Wang, L. Jia, H. Lin, Y. Zhang, Single-Atomic Catalysts Embedded on Nanocarbon Supports for High Energy Density Lithium-Sulfur Batteries, ChemSusChem 13 (2020) 3404–3411.

[22] C. Zhang, R. Du, J.J. Biendicho, M. Yi, K. Xiao, D. Yang, T. Zhang, X. Wang, J. Arbiol, J. Llorca, Y. Zhou, J.R. Morante, A. Cabot, Tubular CoFeP@CN as a Mott–Schottky Catalyst with Multiple Adsorption Sites for Robust Lithium−Sulfur Batteries, Adv. Energy Mater. 11 (2021) 2100432.

[23] Y. Hwa, E.J. Cairns, Nanostructured Sulfur and Sulfides for Advanced Lithium/Sulfur Cells, Chemelectrochem 7 (2020) 3927–3942.

[24] J. Wang, J. Zhang, S. Duan, T. Li, L. Jia, H. Liu, L. Li, S. Cheng, H. Hu, M. Huang, H. Hu, S. Zhang, Q. Xiao, H. Lin, Interfacial lithium-nitrogen bond catalyzes sulfide oxidation reactions in high-loading Li₂S cathode, Chem. Eng. J. 429 (2022) 132352.

[25] J. Wang, L. Li, H. Hu, H. Hu, Q. Guan, M. Huang, L. Jia, H. Adenusi, K.V. Tian, J. Zhang, S. Passerini, H. Lin, Toward Dendrite-Free Metallic Lithium Anodes: From Structural Design to Optimal Electrochemical Diffusion Kinetics, ACS Nano 16 (2022) 17729–17760.

[26] L. Sheng, Q. Wang, X. Liu, H. Cui, X. Wang, Y. Xu, Z. Li, L. Wang, Z. Chen, G.L. Xu, J. Wang, Y. Tang, K. Amine, H. Xu, X. He, Suppressing electrolyte-lithium metal reactivity via Li⁺-desolvation in uniform nano-porous separator, Nat. Commun. 13 (2022) 172.

[27] H. Tu, L. Li, Z. Wang, J. Wang, H. Lin, M. Wang, C. Yan, M. Liu, Tailoring Electrolyte Solvation for LiF-Rich Solid Electrolyte Interphase toward a Stable Li Anode, ACS Nano 16 (2022) 16898–16908.

[28] X. Zhang, X. Li, Y. Zhang, X. Li, Q. Guan, J. Wang, Z. Zhuang, Q. Zhuang, X. Cheng, H. Liu, J. Zhang, C. Shen, H. Lin, Y. Wang, L. Zhan, L. Ling, Accelerated Li⁺ Desolvation for Diffusion Booster Enabling Low-Temperature Sulfur Redox Kinetics via Electrocatalytic Carbon-Grazfted-CoP Porous Nanosheets, Adv. Funct. Mater. 33 (2023) 2302624.

[29] G. Rong, X. Zhang, W. Zhao, Y. Qiu, M. Liu, F. Ye, Y. Xu, J. Chen, Y. Hou, W. Li, W. Duan, Y. Zhang, Liquid-Phase Electrochemical Scanning Electron Microscopy for In Situ Investigation of Lithium Dendrite Growth and Dissolution, Adv. Mater. 29 (2017) 1606187.

[30] Z.L. Xu, J.Q. Huang, W.G. Chong, X. Qin, X. Wang, L. Zhou, J.K. Kim, In Situ TEM Study of Volume Expansion in Porous Carbon Nanofiber/Sulfur Cathodes with Exceptional High-Rate Performance, Adv. Energy Mater. 7 (2017) 1602078.

[31] Y. Qiu, G. Rong, J. Yang, G. Li, S. Ma, X. Wang, Z. Pan, Y. Hou, M. Liu, F. Ye, W. Li, Z.W. Seh, X. Tao, H. Yao, N. Liu, R. Zhang, G. Zhou, J. Wang, S. Fan, Y. Cui, Y. Zhang, Highly Nitridated Graphene-Li₂S Cathodes with Stable Modulated Cycles, Adv. Energy Mater. 5 (2015) 1501369.

[32] M.U. Patel, I. Arcon, G. Aquilanti, L. Stievano, G. Mali, R. Dominko, X-ray absorption near-edge structure and nuclear magnetic resonance study of the lithium-sulfur battery and its components, Chemphyschem 15 (2014) 894–904.

[33] L. Zhang, D. Sun, J. Feng, E.J. Cairns, J. Guo, Revealing the Electrochemical Charging Mechanism of Nanosized Li2S by in Situ and Operando X-ray Absorption Spectroscopy, Nano Lett. 17 (2017) 5084–5091.

[34] L. Jia, J. Wang, S. Ren, G. Ren, X. Jin, L. Kao, X. Feng, F. Yang, Q. Wang, L. Pan, Q. Li, Y.s. Liu, Y. Wu, G. Liu, J. Feng, S. Fan, Y. Ye, J. Guo, Y. Zhang, Unraveling Shuttle Effect and Suppression Strategy in Lithium/Sulfur Cells by In Situ/Operando X-ray Absorption Spectroscopic Characterization, Energy Environ. Mater. 4 (2020) 222–228.

[35] P. Niehoff, S. Passerini, M. Winter, Interface investigations of a commercial lithium ion battery graphite anode material by sputter depth profile X-ray photoelectron spectroscopy, Langmuir 29 (2013) 5806–5816.

[36] J. Wang, S. Cheng, W. Li, L. Jia, Q. Xiao, Y. Hou, Z. Zheng, H. Li, S. Zhang, L. Zhou, M. Liu, H. Lin, Y. Zhang, Robust electrical "highway" network for high mass loading sulfur cathode, Nano Energy 40 (2017) 390–398.

[37] J. Wang, H. Hu, S. Duan, Q. Xiao, J. Zhang, H. Liu, Q. Kang, L. Jia, J. Yang, W. Xu, H. Fei, S. Cheng, L. Li, M. Liu, H. Lin, Y. Zhang, Construction of Moisture-Stable Lithium Diffusion-Controlling Layer toward High Performance Dendrite-Free Lithium Anode, Adv. Funct. Mater. 32 (2021) 2110468.

[38] J. Xu, W. Tang, C. Yang, I. Manke, N. Chen, F. Lai, T. Xu, S. An, H. Liu, Z. Zhang, Y. Cao, N. Wang, S. Zhao, D. Niu, R. Chen, Highly Conductive COF@CNT Electrocatalyst Boosting Polysulfide Conversion for Li–S Chemistry, ACS Energy Lett. 6 (2021) 3053–3062.

[39] Y.R. Shen, Surface-Properties Probed by 2nd-Harmonic and Sum-Frequency Generation, Nature 337 (1989) 519–525.

[40] K.B. Eisenthal, Liquid Interfaces Probed by Second-Harmonic and Sum-Frequency Spectroscopy, Chem. Rev. 96 (1996) 1343–1360.

[41] S. Baldelli, Probing electric fields at the ionic liquid-electrode interface using sum frequency generation spectroscopy and electrochemistry, J. Phys. Chem. B 109 (2005) 13049–13051.

[42] P. Mukherjee, A. Lagutchev, D.D. Dlott, In Situ Probing of Solid-Electrolyte Interfaces with Nonlinear Coherent Vibrational Spectroscopy, J. Electrochem. Soc. 159 (2012) A244–A252.

[43] B.G. Nicolau, N. García-Rey, B. Dryzhakov, D.D. Dlott, Interfacial Processes of a Model Lithium Ion Battery Anode Observed, in Situ, with Vibrational Sum-Frequency Generation Spectroscopy, J. Phys. Chem. C 119 (2015) 10227–10233.

[44] Y. Horowitz, H.L. Han, P.N. Ross, G.A. Somorjai, In Situ Potentiodynamic Analysis of the Electrolyte/Silicon Electrodes Interface Reactions–A Sum Frequency

Generation Vibrational Spectroscopy Study, J. Am. Chem. Soc. 138 (2016) 726–729.

[45] N.M. Adhikari, U.I. Premadasa, K.L.A. Cimatu, Sum frequency generation vibrational spectroscopy of methacrylate-based functional monomers at the hydrophilic solid-liquid interface, Phys. Chem. Chem. Phys. 19 (2017) 21818–21828.

[46] Y. Xi, Q. Xiao, J. Du, X. Ye, X. Kong, Z. Chang, T. Li, H. Jin, J. Wang, H. Lin, Flow Alters the Interfacial Reactions of Upconversion Nanocrystals Probed by In Situ Sum Frequency Generation, Adv. Mater. Interfaces 7 (2020) 1902046.

[47] J. Wang, H. Hu, J. Zhang, L. Li, L. Jia, Q. Guan, H. Hu, H. Liu, Y. Jia, Q. Zhuang, S. Cheng, M. Huang, H. Lin, Hydrophobic lithium diffusion-accelerating layers enables long-life moisture-resistant metallic lithium anodes in practical harsh environments, Energy Storage Mater. 52 (2022) 210–219.

[48] L. Yu, H. Liu, Y. Wang, N. Kuwata, M. Osawa, J. Kawamura, S. Ye, Preferential adsorption of solvents on the cathode surface of lithium ion batteries, Angew. Chem. Int. Ed. Engl. 52 (2013) 5753–5756.

[49] D. Verreault, V. Kurz, C. Howell, P. Koelsch, Sample cells for probing solid/liquid interfaces with broadband sum-frequency-generation spectroscopy, Rev. Sci. Instrum. 81 (2010) 063111.

[50] C.D. Bain, Sum-frequency vibrational spectroscopy of the solid/liquid interface, Fara. Trans. 91 (1995) 1281–1296.

[51] J. Wang, S. Cheng, W. Li, S. Zhang, H. Li, Z. Zheng, F. Li, L. Shi, H. Lin, Y. Zhang, Simultaneous optimization of surface chemistry and pore morphology of 3D graphene-sulfur cathode via multi-ion modulation, J. Power Sources 321 (2016) 193–200.

[52] Y. Qiu, W. Li, W. Zhao, G. Li, Y. Hou, M. Liu, L. Zhou, F. Ye, H. Li, Z. Wei, S. Yang, W. Duan, Y. Ye, J. Guo, Y. Zhang, High-Rate, Ultralong Cycle-Life Lithium/Sulfur Batteries Enabled by Nitrogen-Doped Graphene, Nano Lett. 14 (2014) 4821–4827.

[53] H. Pan, J. Chen, R. Cao, V. Murugesan, N.N. Rajput, K.S. Han, K. Persson, L. Estevez, M.H. Engelhard, J.G. Zhang, K.T. Mueller, Y. Cui, Y. Shao, J. Liu, Non-encapsulation approach for high-performance Li–S batteries through controlled nucleation and growth, Nat. Energy 2 (2017) 813–820.

[54] X. Song, T. Gao, S. Wang, Y. Bao, G. Chen, L.X. Ding, H. Wang, Free-standing sulfur host based on titanium-dioxide-modified porous-carbon nanofibers for lithium-sulfur batteries, J. Power Sources 356 (2017) 172–180.

[55] L. Ji, M. Rao, H. Zheng, L. Zhang, Y. Li, W. Duan, J. Guo, E.J. Cairns, Y. Zhang, Graphene oxide as a sulfur immobilizer in high performance lithium/sulfur cells, J. Am. Chem. Soc. 133 (2011) 18522–18525.

[56] J. Wang, L. Jia, H. Liu, C. Wang, J. Zhong, Q. Xiao, J. Yang, S. Duan, K. Feng, N. Liu, W. Duan, H. Lin, Y. Zhang, Multi-ion Modulated Single-Step Synthesis of a Nanocarbon Embedded with a Defect-Rich Nanoparticle Catalyst for a High Loading Sulfur Cathode, ACS Appl. Mater. Interfaces 12 (2020) 12727–12735.

[57] Y. Zhang, G. Xu, Q. Kang, L. Zhan, W. Tang, Y. Yu, K. Shen, H. Wang, X. Chu, J. Wang, S. Zhao, Y. Wang, L. Ling, S. Yang, Synergistic electrocatalysis of polysulfides by a nanostructured VS4-carbon nanofiber functional separator for high-performance lithium–sulfur batteries, J. Mater. Chem. A 7 (2019) 16812–16820.

[58] B. Bozzini, A. Bund, B. Busson, C. Humbert, A. Ispas, C. Mele, A. Tadjeddine, An SFG/DFG investigation of CN− adsorption at an Au electrode in 1-butyl-1-methyl-pyrrolidinium bis(trifluoromethylsulfonyl) amide ionic liquid, Electrochem. Commun. 12 (2010) 56–60.

[59] M. Herstedt, M. Smirnov, P. Johansson, M. Chami, J. Grondin, L. Servant, J. C. Lassègues, Spectroscopic characterization of the conformational states of the bis (trifluoromethanesulfonyl)imide anion (TFSI−), J. Raman Spectrosc. 36 (2005) 762–770.

[60] M. Castriota, T. Caruso, R.G. Agostino, E. Cazzanelli, W.A. Henderson, S. Passerini, Raman investigation of the ionic liquid N-methyl-N-propylpyrrolidinium bis (trifluoromethanesulfonyl)imide and its mixture with LiN(SO₂CF₃)₂, J. Phys. Chem. A 109 (2005) 92–96.

[61] D.M. Seo, P.D. Boyle, R.D. Sommer, J.S. Daubert, O. Borodin, W.A. Henderson, Solvate structures and spectroscopic characterization of LiTFSI electrolytes, J. Phys. Chem. B 118 (2014) 13601–13608.

[62] R. Chen, F. Wu, L. Li, X. Qiu, L. Chen, S. Chen, The structure–activity relationship studies of binary room temperature complex electrolytes based on LiTFSI and organic compounds with acylamino group, Vib. Spectrosc. 44 (2007) 297–307.

[63] Y. Hu, Z. Wang, H. Li, X. Huang, L. Chen, Spectroscopic and DFT studies to understand the liquid formation mechanism in the LiTFSI/acetamide complex system, Spectrochim. Acta A Mol. Biomol Spectrosc. 61 (2005) 2009–2015.

[64] T. Iwahashi, T. Miyamae, K. Kanai, K. Seki, D. Kim, Y. Ouchi, Anion configuration at the air/liquid interface of ionic liquid [bmim]OTf studied by sum-frequency generation spectroscopy, J. Phys. Chem. B 112 (2008) 11936–11941.

[65] J. Wang, J. Yang, Q. Xiao, J. Zhang, T. Li, L. Jia, Z. Wang, S. Cheng, L. Li, M. Liu, H. Liu, H. Lin, Y. Zhang, In Situ Self-Assembly of Ordered Organic/Inorganic Dual-Layered Interphase for Achieving Long-Life Dendrite-Free Li Metal Anodes in LiFSI-Based Electrolyte, Adv. Funct. Mater. 31 (2020) 2007434.

[66] Y. Yang, G. Zheng, S. Misra, J. Nelson, M.F. Toney, Y. Cui, High-capacity micrometer-sized Li₂S particles as cathode materials for advanced rechargeable lithium-ion batteries, J. Am. Chem. Soc. 134 (2012) 15387–15394.

[67] J. Zhang, L. Jia, H. Lin, J. Wang, Advances and Prospects of 2D Graphene-Based Materials/Hybrids for Lithium Metal–Sulfur Full Battery: From Intrinsic Property to Catalysis Modification, Adv. Energy Sustain. Res. 3 (2022) 2100187.

[68] S. Cheng, J. Wang, S. Duan, J. Zhang, Q. Wang, Y. Zhang, L. Li, H. Liu, Q. Xiao, H. Lin, Anionic oxygen vacancies in Nb₂O₅₋ₓ/carbon hybrid host endow rapid catalytic behaviors for high-performance high areal loading lithium sulfur pouch cell, Chem. Eng. J. 417 (2021) 128172.

[69] S. Jeong, D. Bresser, D. Buchholz, M. Winter, S. Passerini, Carbon coated lithium sulfide particles for lithium battery cathodes, J. Power Sources 235 (2013) 220–225.